Model Order Reduction of Wind Farms: Linear Approach

Husni Rois Ali, Linash P. Kunjumuhammed, *Senior Member IEEE*, Bikash C. Pal, *Fellow, IEEE*, Andrzej G Adamczyk *Member, IEEE*, and Konstantin Vershinin *Member, IEEE*

***Abstract*—This paper presents three types of linear model order reduction (MOR) technique, namely singular value decomposition (SVD)-based, Krylov-based, and modal truncation-based type applied to large-scale wind farm models. The first type includes a Balanced Truncation (BT) and Alternating Direction Implicit (ADI)-based BT method, while the second type encompasses a Rational Krylov (RK), and Iterative Rational Krylov Algorithm (IRKA) method. In the third type, a Subspace Accelerated MIMO Dominant Pole Algorithm (SAMDP) method is used. The effectiveness of these methods are tested on practical-sized wind farms with 90, 120 and 210 doubly-fed induction generators (DFIGs). Merits and demerits of each method are discussed in detail. The reduced order model (ROM) of wind farm is validated against the full order model (FOM) in term of frequency domain indices and waveform agreement at the point of common coupling (PCC).**

***Index Terms*—wind farm model order reduction, Balanced Truncation, Alternating Direction Implicit-based BT, Rational Krylov, Iterative Rational Krylov Algorithm, Subspace Accelerated MIMO Dominant Pole Algorithm (SAMDP).**

I. Introduction

OVER the past twenty years, there has been phenomenal growth in installed capacity of wind power worldwide [1]. Such growth has not been possible without meeting various challenges. Most often these problems are related to grid interconnection, so analysis of wind farm connected to external grids are required to understand such problems and seek appropriate solutions.

A detailed dynamic model of a typical wind turbine generator (WTG) may be described using about 20 differential equations. Inevitably, representation of a medium size wind farm consisting of about 100 WTGs in power system study requires thousands of differential equations. With the inclusion of collector system component dynamics such as cable sections and transformers, the overall model order becomes extremely large to handle in power system simulation studies. However, such detailed representation poses computational burden for typical power system simulation software, preventing the study of behaviour of wind farms connected to a power system virtually infeasible. Hence, a reduced model of wind farm, which can capture important dynamics of the high order system, is of importance for power system study. In addition to computational issue, for control engineers, reducing dynamic model of complex systems has become an integral part of controller design [2]. A complex model leads to not only a complex controller design but also a high cost and also poor reliability. With a reduced order wind farm model, a simple controller design can be easily pursued. For developers and WTG manufacturers, this reduced model of WF is also useful to demonstrate and validate stability of their system and equipment while safe guarding their intellectual properties.

In order to obtain the reduced order model of wind farms, the aggregation-based method, which was originally used in synchronous machines model, is by far the most popular method [3], [4], [5]. The method can be further divided into the single-machine and multiple-machine aggregation. In the former method [3], it is assumed that the whole wind farm operates at uniformly in wind speed and power output terms; thus an aggregated WTG is sufficient to represent the dynamics of wind farms. Since wind farms are normally situated across a very large area, this assumption can be hardly fulfilled due to the wake effects, size of each WTG, etc. Consequently, the single-machine aggregation cannot accurately represent the dynamics of a wind farm. To overcome this problem, the multi-machine representation is used. In this method, the WTGs are grouped according to the similarity of operating condition, known as a coherent group, and the generators with a similar operating condition are represented by an equivalent model [4], [5]. Despite its popularity in the literature, multi-machine aggregation has several weaknesses: 1) The operating condition of wind farm is continuously changing, as a result a coherent group of WTGs may contain different set of generators, 2) Unlike synchronous generators where the concept of coherent group is well defined by the rotor angle, in WTGs, this is not easy due to the weak connection between rotor angle and WTG's output power.

In this paper, the application of linear reduced order model (ROM) techniques, which do not rely on identification of coherent group of WTGs, is demonstrated on practical-sized wind farm models [6]. The methods include Balanced Truncation (BT) [7], Alternating Direction Implicit (ADI)-based BT [8], [9], [10], Rational Krylov (RK) [8], [11], Iterative Rational Krylov Algorithm (IRKA) [12], [13] and Subspace Accelerated MIMO Dominant Pole Algorithm (SAMDP) [14]. To the knowledge of the authors, the last four methods are the first of their kind in wind farm MOR. Applicability and effectiveness of these five methods are compared and contrasted. The reduced order models are validated by comparing eigenvalues, bode plots and dynamic response waveform with those from the the full order model (FOM).

Husni Rois Ali, L. P. Kunjumuhammed and B. C. Pal are with the Department of Electrical and Electronic Engineering, Imperial College, London SW7 2AZ, U.K. (e-mail: {h.ali15;linash.p.k; b.pal}@imperial.ac.uk)

Andrzej Adamczyk and Konstantin Vershinin are with the GE′s Grid Solutions, St Leonards Building Harry Kerr Drive Stafford ST16 1WT (e-mail: {andrzej.adamczyk;konstantin.vershinin}@ge.com).

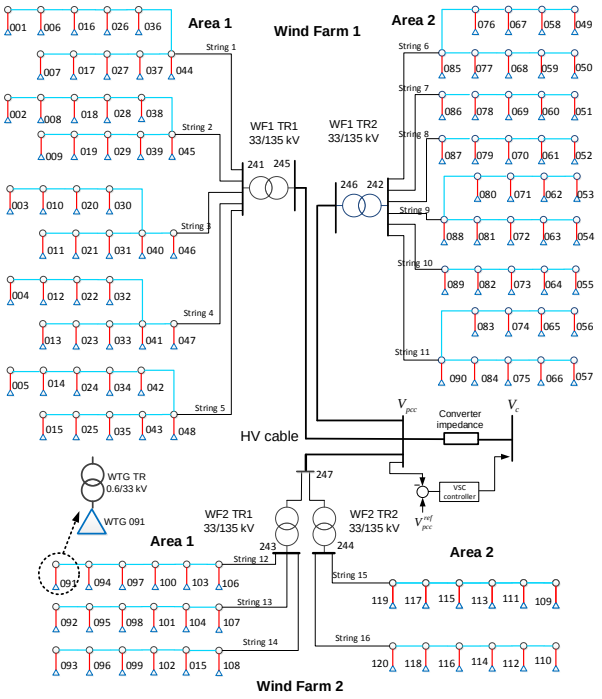

Fig. 1: Wind farm connected to grid

II. Approach for Wind Farm Model Order Reduction

The basic layout of a 120×5 MW wind farm used in this research is shown in Fig. 1. This layout will be modified in Section V to investigate the reliability of MOR techniques for different sizes of test systems. In Fig. 1, triangles indicate DFIG type WTG. The model is divided into two wind farms, namely Wind Farm 1 and 2, where each has several strings of WTGs connected to a wind farm transformer (WFT). The WFTs are connected to Voltage Source Converter (VSC)-HVDC using three high voltage cables (HVCs). The DC-link of the HVDC that connects wind farm to main grid is not considered in this work. The dynamic model of a DFIG uses a 22^{nd} order model. The converter controllers use a vector control approach to allow independent control of torque and reactive power [15]. Each collector system component is represented using a fourth order model [6].

The system is modelled using Matlab/Simulink® and linear representation is obtained using the command *linearise*. The order of system is 3874 with 1673 conjugate pairs of eigenvalue. The frequency of the modes ranges from 1.7 Hz to 3.5×10^4 Hz. The lower frequency modes are related to DFIG's mechanical system, while the higher frequency modes are due to a capacitor-inductor combination in the collector system. The model contains four critical modes listed in Table I. Using the $q-$axis of PCC voltage and $d-$axis of converter voltage as the input and output, respectively, these modes are evident as significant peaks in the Bode plot magnitude given in Fig. 2. Further, a nonlinear time domain simulation is performed by applying a 1% step change in the PCC reference voltage at $t = 0.3$ s. Fig 3 shows the responses of PCC active power and voltage, which are dominated by the critical modes.

To perform MOR, the wind farm system is partitioned into two areas [16], namely, *study-area* and *external-area* as

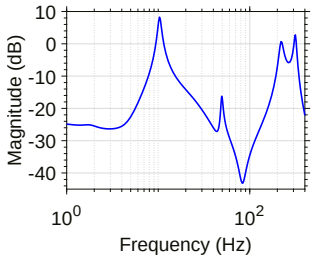

Fig. 2: Bode magnitude plot for full order model of the wind farm

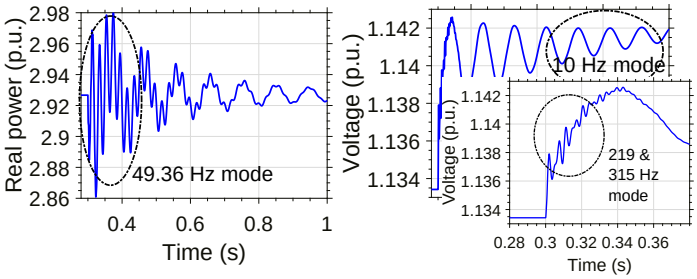

(a) Active power at PCC (b) Voltage at PCC

Fig. 3: Response due to a fault at PCC voltage reference

illustrated in Fig. 4. The wind farm with the collector systems is considered as the *external-area*, and the *study-area* includes only the VSC controller and impedance. The *external-area* is linearised and subsequently reduced using the methods presented in Section III. The ROM is reconnected to study area, and its response is compared to the response of wind farm FOM using the following three criteria:

1) The critical modes of both systems are compared.
2) The Bode plot of both systems is compared specifically around the frequency of critical modes.
3) The PCC power and voltage of both system are compared using Mean Square Error (MSE),

$$\text{MSE} = \left(\sum_{n=1}^{N} \sum_{t=1}^{T} (y_{n,t} - \hat{y}_{n,t})^2 / NT \right)^{1/2} \tag{1}$$

where y and $\hat{y}$ denote output of the FOM and ROM, respectively. N is the number of outputs to be compared, and T is total number of time steps.

III. Model Order Reduction Methods

To obtain a linear model, the nonlinear model in Fig. 1 is linearised around an operating condition $x(0)$, $y(0)$ and $u(0)$,

$$\dot{x}(t) = Ax(t) + Bu(t),\ y(t) = Cx(t) + Du(t) \tag{2}$$

where $A \in R^{n\times n}$, $B \in R^{n\times m}$, $C \in R^{k\times n}$, and $D \in R^{k\times m}$ are the state, input, output, and feedforward matrices, respectively, while $x(t) \in R^n, y(t) \in R^k$, and $u(t) \in R^m$ denote state, output, and input vectors, respectively. In the wind farm system studied, matrix D is zero. The transfer function of (2) is expressed as,

$$G(s) = \left[\begin{array}{c|c} A & B \\ \hline C & D \end{array}\right] = C(sI - A)^{-1}B + D \tag{3}$$

$G(s)$ is controllable if for an initial states $x(-\infty)$, there is input $u(t)$ that brings the initial states $x(-\infty)$ to $x(0)$. This is

TABLE I
CRITICAL MODES OF FULL ORDER SYSTEM

Mode	Frequency (Hz)	Damping (%)	Dominant states
M1	315	2.9	V_{PCC}, I_{VSC}, V_{HVC}, I_{WFT}
M2	220	5.1	V_{PCC}, I_{VSC}, V_{HVC}, I_{WFT}
M3	49.36	2.6	I_{VSC}
M4	10.33	4.2	I_{VSC}, I_{WFT}, V_{PCC}, VSC controller states

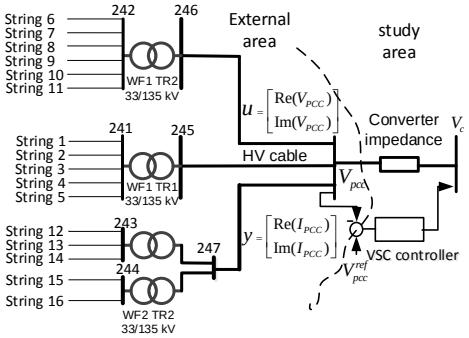

Fig. 4: Model order reduction approach

equivalent to controllability Gramian P defined by (4) being positive definite,

$$P = \int_0^\infty e^{-At} B B^T e^{-A^T t} dt \tag{4}$$

P is the solution to the Lyapunov equation,

$$AP + A^T P + BB^T = 0 \tag{5}$$

Further by assuming that $x(-\infty) = 0$, P is related to the energy to control states,

$$\|u(t)\|_2^2 = x(0)^T P^{-1} x(0) \tag{6}$$

If the SVD is performed on P, small singular values correspond to the states which are difficult to control.

Similar to controllability, $G(s)$ is observable if given the values of $u(t)$ and $y(t)$ for any $t \geq 0$, it is possible to determine a unique initial state $x(0)$ [17]. This can be checked by using observability Gramian defined as,

$$Q = \int_0^\infty e^{A^T t} C^T C A^{At} dt \tag{7}$$

If Q is positive-definite, then the system is observable. Q is the solution to the Lyapunov equation,

$$A^T Q + QA + C^T C = 0 \tag{8}$$

It is related to the energy observation of states. Suppose that an autonomous system is released from initial states $x(0)$, the energy of $y(t)$ can be computed using,

$$\|y(t)\|_2^2 = x(0)^T Q x(0) \tag{9}$$

If SVD is performed on Q, small singular values are related to the states which are difficult to observe.

To obtain ROM of $G(s)$, the state variables $x(t) \in R^n$ is projected into a new set of state variables $\hat{x}(t) \in R^r$ with $r << n$ by using a projection matrix $V \in R^{n \times r}$

$$x(t) \approx V \hat{x}(t) \tag{10}$$

It is often imposed that the error of this approximation must be perpendicular to a subspace $W \in R^{n \times r}$, where $W^T V = I_r$. The ROM is obtained through substituting (10) into (2) and pre-multiplying the result with W^T,

$$\dot{\hat{x}}(t) = \hat{A}\hat{x}(t) + \hat{B}u(t),\ y(t) = \hat{C}\hat{x}(t) + \hat{D}u(t) \tag{11}$$

where: $\hat{A} = W^T A V$, $\hat{B} = W^T B$, $\hat{C} = CV$, $\hat{D} = D$. In subsequent sections, five different methods to obtain $\hat{G}(s)$ from $G(s)$ will be discussed.

A. Balanced truncations (BT)

As previously stated, the small singular values of P and Q correspond to the states which are difficult to control and observe, respectively. These states do not participate significantly in the input-output behavior and as a result they can be eliminated. However, the states which are difficult to observe do not necessarily concur with the states which are difficult to control [2]. Thus, a coordinate transformation is required to transform $G(s)$ into a new coordinate system $\tilde{G}(s)$,

$$\tilde{G}(s) = \left[\begin{array}{c|c} \tilde{A} & \tilde{B} \\ \hline \tilde{C} & \tilde{D} \end{array}\right] = \left[\begin{array}{c|c} T^{-1}AT & T^{-1}B \\ \hline CT & D \end{array}\right] \tag{12}$$

In this new coordinate system, the controllability and observability Gramian are equivalent,

$$\begin{aligned} &TPT^T = T^{-T} Q T^{-1} \\ &\tilde{P} = \tilde{Q} = \Sigma_H = \text{diag}(\sigma_1,\ \cdots\ \sigma_n),\ \sigma_1 \geq\ \cdots \geq\ \sigma_n \end{aligned} \tag{13}$$

The term σ_i are known as Hankel singular values (HSV). The HSV represent the energy of states connecting inputs and outputs and it is normally arranged in descending order. The transformation matrix T used in (12) is given by

$$T = R^T U \Sigma^{1/2},\ T^{-1} = R U \Sigma^{-1/2} \tag{14}$$

where R is the Cholesky factor of P and Σ is the singular values of RQR^T given by,

$$P = R^T R,\ RQR^T = U \Sigma^2 U^T \tag{15}$$

The balance system $\tilde{G}(s)$ can be partitioned according to partition of Σ_H,

$$\Sigma_H = \left[\begin{array}{c|c} \Sigma_{H1} & \\ \hline & \Sigma_{H2} \end{array}\right] \tag{16}$$

Σ_{H1} represents HSVs with significantly large magnitudes. This partition yields,

$$\tilde{G}(s) = \left[\begin{array}{cc|c} \tilde{A}_{11} & \tilde{A}_{12} & \tilde{B}_1 \\ \tilde{A}_{21} & \tilde{A}_{22} & \tilde{B}_2 \\ \hline \tilde{C}_1 & \tilde{C}_2 & \tilde{D} \end{array}\right] \tag{17}$$

The ROM $\hat{G}(s)$ is obtained by preserving sub-matrices as follows,

$$\hat{G}(s) = \left[\begin{array}{c|c} \tilde{A}_{11} & \tilde{B}_1 \\ \hline \tilde{C}_1 & \tilde{D} \end{array}\right] \tag{18}$$

It has been shown in [2] that if Σ_{H1} and Σ_{H2} have no common terms or entries, then (18) is always stable with the error bound expressed by,

$$\left\| G(s) - \hat{G}(s) \right\|_\infty \leq 2(\sigma_{r+1}\ \sigma_{r+1} \cdots \sigma_n) \tag{19}$$

This is known as *the twice sum of a tail rule* [18], which states that accuracy of the ROM in (18) increases when more HSVs are included.

B. Alternating Directions Implicit (ADI)-based BT

The BT presented in the previous section has been widely used for reducing the order of dynamic systems. Unfortunately, as presented in Section IV, its application is restricted to small to medium-sized systems due to the fact that the cost of solving two Lyapunov equations in (5) and (8) is prohibitive. To deal with this problem, an Alternating Direction Implicit (ADI)-based algorithm is proposed to reduce the complexity of BT by solving Lyapunov equation iteratively, which allows extension of BT for wind farm systems.

The ADI iteration was originally used to solve a system of linear equations as given in Appendix A. To solve Lyapunov equation using ADI, (37) can be directly applied to (5) and (8). As these equations are dual, it will only be illustrated for (5). To conform with the ADI procedure, (5) is rewritten as $AP + A^T P = -BB^T$. Hence, ADI iteration for this equation is,

$$\begin{aligned} (A + \alpha_i I_n) P_{i-\frac{1}{2}} &= -P_{i-1}(A^T - \alpha_i I_n) - BB^T \\ (A + \alpha_i I_n) P_i^T &= -P_{i-\frac{1}{2}}^T (A^T - \alpha_i I_n) - BB^T \end{aligned} \tag{20}$$

Combining two equations above into single equation yields,

$$\begin{aligned} P_i = &(A + \alpha_i I_n)^{-1}(A - \bar{\alpha}_i I_n) P_{i-1} (A - \bar{\alpha}_i I_n)^T (A + \alpha_i I_n)^{-T} \\ &- \text{Re}(\alpha_i)(A + \alpha_i I_n)^{-1} B B^T (A + \alpha_i I_n)^{-T} \end{aligned} \tag{21}$$

Using (21) with the proper shift parameters α_i, P can be found efficiently. Further, realizing the fact that in BT, the aim is to calculate a low-rank factorization of P i.e. R as in 15, it is possible to modify (21) to directly calculate R [19]. Assuming that $R_0 = 0$ and $R_i R_i^T = P_i$, then (21) can be rewritten as,

$$\begin{aligned} R_1 =& \sqrt{-\text{Re}(\alpha_1)}(A+\alpha_1 I_n)^{-1}B \\ R_i =& \Big[\sqrt{-\text{Re}(\alpha_1)}(A+\alpha_1 I_n)^{-1}B,\ (A+\alpha_i I_n)^{-1}(A-\bar{\alpha_i} I_n)R_{i-1}\Big] \end{aligned} \tag{22}$$

The shift parameters used in (37)-(21) are obtained from the solution of a min-max problem,

$$\alpha_i = \min_{\substack{\alpha_i \in \mathbb{C}_{<0}, \\ i=1,\dots,J}} \max_{\lambda \in \Lambda(A)} = \prod_{i=1}^{J} \frac{|\alpha_i - \lambda|^2}{|\alpha_i + \lambda|^2} \tag{23}$$

Several methods are available to solve this [20], [21]. One of the challenges is to calculate the spectrum of A as for a large system calculating this spectrum is computationally expensive. In this research, the heuristic approach proposed in [20] is followed. The spectrum of A is approximated by using Arnoldi iteration and then (23) is solved heuristically.

C. Rational Krylov (RK)

The method presented in this section is based on moment matching via Krylov subspace, which is specifically known as Rational Krylov (RK). As shown in Section IV, selecting a set of interpolation points, denoted as σ_i, is crucial for the accuracy of RK. These points are often selected from the mirror image of dominant poles [13]. Given a single-input single-output (SISO) system with the transfer function in (3), it can be expanded around infinity ($\sigma \approx \infty$),

$$G(s) = \sum_{i=1}^{\infty} m_i s^{-i}, \text{with } m_i = CA^{i-1}B \tag{24}$$

The term m_i is known as i^{th} moment of the transfer function. In more general cases, $G(s)$ may be also expanded at $\sigma \neq \infty$,

$$\begin{aligned} G(s) &= \sum_{i=0}^{\infty} m_i (s-\sigma)^i \\ \text{with } m_i(\sigma) &= CA^{-(i+1)}B, \text{ for } \sigma = 0 \text{ or} \\ m_i(\sigma) &= C(\sigma I - A)^{-(i+1)}B, \text{ for } \sigma \neq 0 \text{ or } \infty \end{aligned} \tag{25}$$

Approximation of $G(s)$ by $\hat{G}(s)$ is carried out by preserving k moments of the original system such that $m_i = \hat{m}_i,\ i = 1, 2, ...k$. The term $\hat{m}_i$ denotes the moments of $\hat{G}(s)$. In the RK, the moments are not computed explicitly to avoid the risk of numerical non-convergence because of ill-conditioning. Moment matching is instead performed via projection onto a Krylov subspace, which is defined as,

$$\mathcal{K}_q(A, B) = \text{span}\left\{B, \quad AB, \quad A^2B, \quad \cdots, \quad A^{q-1}B\right\} \tag{26}$$

If V and W in (11) are selected to span a certain Kylov subspace, then the moments of FOM m_i are automatically preserved in the ROM. The preservation are selected from [8], [11]:

1) If $\text{span}(V) = \mathcal{K}_{q1}(A, B)$ and $\text{span}(W) = \mathcal{K}_{q2}(A^T, C^T)$, then $\hat{G}(s)$ preserves $q1 + q2$ moments of $G(s)$ at infinity.
2) If $\text{span}(V) = \mathcal{K}_{q1}(A^{-1}, A^{-1}B)$ and $\text{span}(W) = \mathcal{K}_{q1}(A^{-T}, A^{-T}C^T)$, then $\hat{G}(s)$ preserves $q1 + q2$ moments of $G(s)$ at zero.
3) If $\text{span}(V) = \mathcal{K}_{q1}((A-\sigma I)^{-1}, (A-\sigma I)^{-1}B)$ and $\text{span}(W) = \mathcal{K}_{q1}((A-\sigma I)^{-T}, (A-\sigma I)^{-T}C^T)$, then $\hat{G}(s)$ preserves $q1 + q2$ moments of $G(s)$ at σ.
4) If σ in point 2) and 3) is multi-point i.e. $\sigma = [\sigma_1, ..., \sigma_i]$, by taking V and W as a union of Krylov subspaces corresponding to each σ_i, then $\hat{G}(s)$ preserves $q1 + q2$ moments of $G(s)$ at σ_i. This is known as generalized Krylov subspaces.

Although the discussion above assumes that the system is SISO, it can be extended to multi-input multi-output (MIMO) system by using block Krylov subspace. This approach is nonetheless only applicable for systems with minimum number of inputs and outputs. Furthermore, it is to be noted if the power of A is continuously multiplied by B as in (26), the resulting vectors will eventually converge to the dominant eigenspace of A. This condition is undesirable due to the fact that the new vector becomes closely parallel to the previous vectors. Consequently, K_j is ill-conditioned. To deal with this condition, the Krylov vector is orthogonalised against previous vectors using Arnoldi and Lanczos methods.

D. Iterative Rational Krylov Algorithm (IRKA)

The operating condition of a system often continuously changes, which may accordingly alter the dominant modes. Hence, interpolation point selection of RK becomes difficult. This section presents an Iterative Rational Krylov Algorithm (IRKA) which can overcome this problem. The IRKA also uses a tangential interpolation method as proposed in [22] to handle MIMO systems.

Suppose $G(s)$ is a MIMO system and a set of z interpolation points with associated right and left tangential directions $\{\sigma_i, r_i, l_i\},\ i = 1, \dots\ z$ are given. If V and W are selected such that,

$$\begin{aligned} (\sigma_i I - A)^{-1}Br_i &= \text{span}(V) \\ (\sigma_i I - A)^{-1}C^T l_i &= \text{span}(W) \end{aligned} \tag{27}$$

then $\hat{G}(s)$ interpolates $G(s)$ tangentially at σ_i and satisfies the following conditions [22], [23],

$$\begin{aligned} l_i^T G(\sigma_i) &= l_i^T \hat{G}(\sigma_i),\ G(\sigma_i)r_i = \hat{G}(\sigma_i)r_i, \\ l_i^T G^{'}(\sigma_i)r_i &= l_i^T \hat{G}^{'}(\sigma_i)r_i,\ \forall i = 1, 2, \dots, z \end{aligned} \tag{28}$$

Equation (28) shows that the IRKA uses a more relaxed condition than exact interpolation in the RK. The remaining problem is how to select $\{\sigma_i, r_i, l_i\}$ appropriately. The IRKA selects $\{\sigma_i, r_i, l_i\}$ to minimise H_2 norm error between $G(s)$ and $\hat{G}(s)$,

$$\min \left\| G(s) - \hat{G}(s) \right\|_2^2 \tag{29}$$

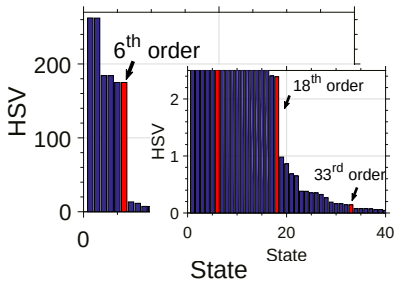

Fig. 5: HSV plot of external area using BT

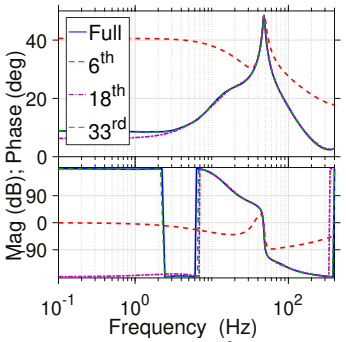

Fig. 6: Bode plot of *external-area* from $\text{Vq}_{\text{pcc}}^{\text{ref}}$ to Id_{pcc}: FOM vs ROM by BT

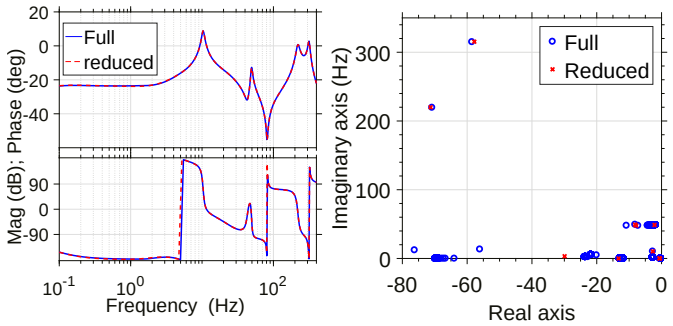

(a) Bode plot from $\text{Vd}_{\text{pcc}}^{\text{ref}}$ to Vq_{pcc} (b) Eigenvalue plot

Fig. 7: Frequency domain comparison of complete system: FOM vs ROM by BT

Let $G(s)$ be expressed in terms of pole-residue representation,

$$G(s) = \sum_{i=1}^{n} \frac{c_i b_i^T}{s - \lambda_i} = \frac{R_i}{s - \lambda_i} \tag{30}$$

where $AX^v = X^v \text{diag}(\lambda_1, ..., \lambda_n)$, $c_i = CX^v e_i$, and $b_i = (e_i^T Y^v B)^T$ with $Y^v = X^{v-1}$. Columns of X^v and Y^v are constructed from the right and left eigenvectors of λ, respectively. A triplet $\{\lambda_i, x_i^v, y_i^v\}$ is commonly referred as an eiganpair. R_i is known as the residue of λ_i. The IRKA tries to find $\hat{G}(s)$,

$$\hat{G}(s) = \sum_{i=1}^{r} \frac{\hat{c}_i \hat{b}_i^T}{s - \hat{\lambda}_i} = \frac{\hat{R}_i}{s - \hat{\lambda}_i} \tag{31}$$

which satisfies (29). The first order optimality conditions for this problem is proposed in [24]. If $\hat{G}(s)$ is the solution of (29), then the following conditions hold,

$$\begin{aligned} &\hat{c}_i^T G(-\hat{\lambda}_i) = \hat{c}_i^T \hat{G}(-\hat{\lambda}_i),\ G(-\hat{\lambda}_i)\hat{b}_i = \hat{G}(-\hat{\lambda}_i)\hat{b}_i \\ &\hat{c}_i^T G'(-\hat{\lambda}_i)\hat{b}_i = \hat{c}_i^T \hat{G}'(-\hat{\lambda}_i)\hat{b}_i,\ \forall i = 1, \ldots, r \end{aligned} \tag{32}$$

where $\hat{\lambda}_i$ are poles of $\hat{G}(s)$ with associated residues $\hat{c}_i, \hat{b}_i$. Therefore, equation (32) suggests that the interpolations points should be selected from mirror image the eigenvalues of ROM, while the corresponding tangential directions are selected from the associated left and right eigenvector.

E. Modal Truncation

In the IRKA, one tries to find $\hat{R}_i$ and $\hat{\lambda}_i$ in (31), so that (29) is minimised. On the other hand, the modal truncation constructs a ROM so that (31) preserves r most dominant eigenvalues of (30). In this way, system stability is always guaranteed to be preserved. One way to define dominant modes is through the corresponding residue R_i of λ_i. A mode λ_i is called dominant if it has a large ratio of $\|R_i\|_2 / |\text{Re}(\lambda_i)|$; thus, the modal truncation selects the r largest ratio.

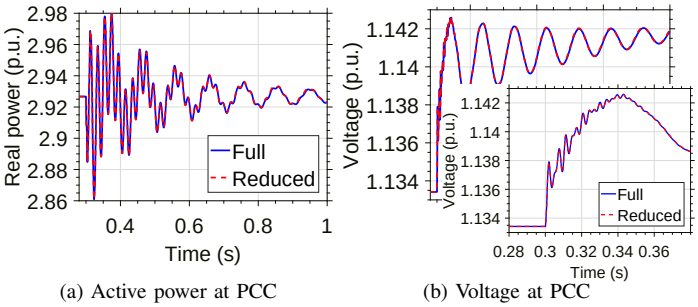

(a) Active power at PCC (b) Voltage at PCC

Fig. 8: Time domain comparison of complete system: FOM vs ROM by BT

When the modal truncation is applied to a large-scale system, the calculation of all eigenpairs $\{\lambda_i, x_i^v, y_i^v\}$ and then selection of dominant modes based on the ratio of $\|R_i\|_2 / |\text{Re}(\lambda_i)|$ become extremely expensive. To overcome this, the eigenpairs $\{\lambda_i, x_i^v, y_i^v\}$ should be calculated one-at-a-time until r eigenpairs are found. In [14], a new method known as a Subspace Accelerated MIMO Dominant Pole Algorithm (SAMDP) has been successfully used to extract dominant modes of large power system models. This method starts from an initial value of a pole and performs iterations until a pole with largest ratio of $\|R_i\|_2 / |\text{Re}(\lambda_i)|$ is found. During the iteration, the corresponding right and left eigenvectors are also calculated. Once this pole has been found, it is deflated to prevent the iterations to converge to the same pole. This process is repeated until r eigenpairs are found. Having completed this process, the right and left eigenvectors are put into columns of V and W, respectively, as follows,

$$W = \left[y_1^v \,\middle|\, \cdots \,\middle|\, y_r^v \right], \quad V = \left[x_1^v \,\middle|\, \cdots \,\middle|\, x_r^v \right] \tag{33}$$

The ROM is obtained by applying V and W to the FOM as in (11).

IV. Wind Farm Model Order Reduction

A. Reduced order model using BT

Prior to reducing the system using the BT, the *external-area* needs to be linearised. This produces a linear system with an order of 3868. Furthermore, it has two inputs (d and q-axis PCC voltage) and also two outputs (d and q-axis PCC current). The *study-area*, by contrast, is retained using nonlinear model.

The order of reduced model is easily determined through inspection of HSV plot shown in Fig. 5. There are significant drops in the magnitudes after the 6^{th}, 18^{th} and 33^{rd} HSV, and they indicate as appropriate orders of reduced system. The Bode plots from $\text{Vq}_{\text{pcc}}^{\text{ref}}$ to Id_{pcc} for these three ROMs are compared with that of the FOM of *external-area* in Fig.6. It is evident that the 6^{th} order system is able to capture the peak at frequency 47.9 Hz, whereas it performs very poorly for other frequency range. Increasing order to 18^{th} and further to 33^{rd} can significantly enhance the accuracy of ROM. This is consistent with the theory of *the twice sum of the tail rule* of BT in (19).

It is important to pause here and discuss stability preservation of BT. As previously discussed, the ROM obtained from BT preserves stability of the FOM if Σ_{H1} and Σ_{H2} in (16) have no common terms or entries. In other words, the stability

TABLE II
PERFORMANCE OF ALL METHODS

Model	Order	Elapsed time (s)	Extraction time(s)	MSE P_{PCC}	MSE V_{PCC}
Full nonlinear	3874	78.18	-	-	-
Full linear	3874	68.54	-	-	-
BT	39	0.27	433	3.77×10^{-4}	2.96×10^{-5}
ADI	39	0.30	19.18	4.80×10^{-5}	2.05×10^{-6}
RK	42	0.44	0.32	4.3×10^{-3}	9.9×10^{-4}
IRKA	42	0.23	7.41	1.45×10^{-5}	1.52×10^{-5}
SAMDP	307	5.10	31.17	2.42×10^{-4}	1.61×10^{-5}

is always preserved when the HSVs are distinct. It can be observed that in case of wind farm model used in this study, the HSVs are always unique. Although Fig. 5 shows that some HSVs appear to be the same, in fact they slightly differ. Hence, this makes it possible to always obtain a stable ROM of wind farm using BT. This is also supported by a large number of experiments. For further analysis, the 33^{rd} order is selected.

In order to study the complete system, the 33^{rd} order is reconnected to the *study-area* and the combined system is then compared to the FOM in term of Bode plot, eigenvalue plot, and waveform agreement. The Bode plots from Vd_{pcc}^{ref} to Vq_{pcc} are given in Fig. 7a and it is clear that they match very accurately. The same information is also conveyed by the eigenvalue plot in Fig. 7b in which the four critical modes can be accurately retained in the ROM. Further, multiple modes at the frequency close to 50 Hz of the FOM are replaced only by just two modes in the ROM. To investigate waveform agreement at the PCC, the *study-area* is perturbed with a 1% step change in the PCC reference voltage at $t = 0.3$ s. The responses of power and voltage waveform for both full and reduced order are depicted in Fig. 8, which indicates the ROM is able to mimic the oscillations of FOM very accurately. The corresponding MSE of power and voltage given in Table II demonstrates accuracy of the ROM. Further, Table II also shows comparison of the elapsed time in order to perform a one second simulation. As anticipated, for the same simulation duration, the 33^{rd} order system only requires $0.27s$, while the nonlinear FOM and linear FOM require $78.18s$ and $68.54s$, respectively.

However, to solve the Lyapunov equations in the BT proves computationally prohibitive for large-scale systems. For the application in wind farm MOR exercise, this computational cost is even more expensive than simulating the full order system for one second as illustrated in Table II. This shows that a special method is required to calculate the solution of Lyapunov equation more efficiently, enabling extension of BT to the high order model of wind farm.

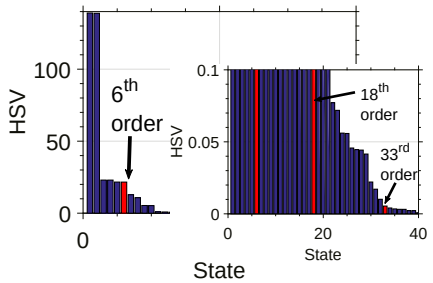

Fig. 9: HSV plot of external area using ADI

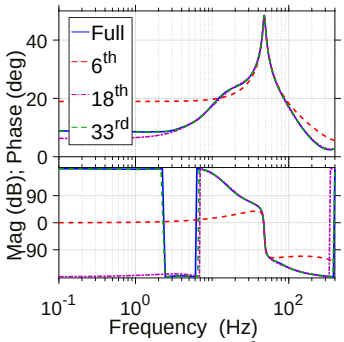

Fig. 10: Bode plot of *external-area* from Vq_{pcc}^{ref} to Id_{pcc}: FOM vs ROM by ADI.

B. Reduced order model using ADI-based BT

The bottleneck of BT is solving the Lyapunov equations. To overcome this, an Alternating Direction Implicit (ADI) iteration is used to solve these equations. A set of shift parameters need to be carefully selected to ensure a satisfactory performance of the ADI method. In this paper, the heuristic approach proposed in [20] is adopted due to its simplicity and Matlab implementation is given in [25]. Since calculating the spectrum of A is computationally prohibitive for large systems, the method estimates these values using the Arnoldi iteration. The spectrum with large magnitudes is determined by performing Arnoldi for 100 iterations, while the spectrum with small magnitudes is calculated by running the same algorithm for 50 iterations and then calculating inverse of the result. The final spectrum, λ, is union of the results from these two processes, but choosing only the values with negative real part. The shift parameters, α_i, is then selected from this final estimation by solving (23) heuristically. The number of shift parameters is set to be 40.

Having obtained the shift parameters, the ADI algorithm is run for 500 iteration. Since there are fewer number of shift parameters than the number of iterations, the shift parameters are used in a cycle. The estimated HSV of the *external-area* is given in Fig. 9. Although the magnitude is different from the exact HSV in Fig. 5, the same orders as in the case of BT, 6, 18, and 33, are selected for the sake of fair comparison. The corresponding HSV is given in Fig. 9. The Bode plots from Vq_{pcc}^{ref} to Id_{pcc} of these three ROMs are compared to that of the FOM of *external-area* in Fig. 10. The 6^{th} order system is only able to capture the peak of full order system at frequency of 47.9 Hz. By increasing the order to 18 and 33, more accurate

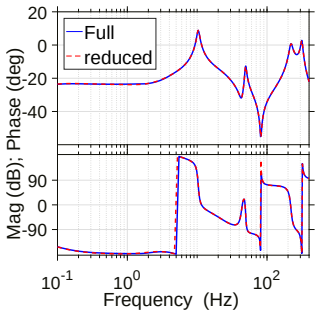

(a) Bode plot from Vd_{pcc}^{ref} to Vq_{pcc}

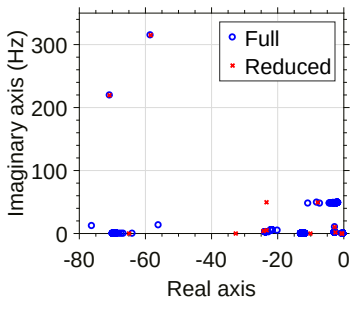

(b) Eigenvalue plot

Fig. 11: Frequency domain comparison of complete system: FOM vs ROM by ADI

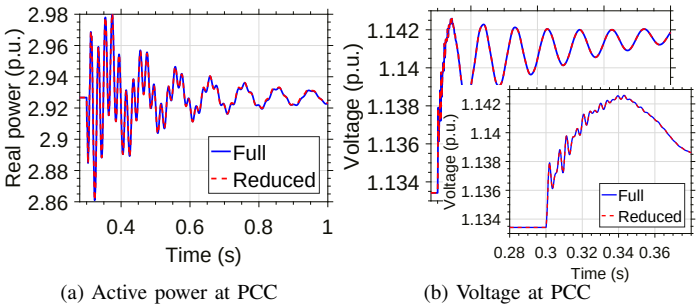

(a) Active power at PCC (b) Voltage at PCC

Fig. 12: Time domain comparison of complete system: FOM vs ROM by ADI

result can be attained. Further analysis is carried out only to the 33^{rd} reduced order system. The Bode and eigenvalue plots of the 33^{rd} ROM when connected to the *study-area* are validated against the FOM and the results are given in Fig. 11. It is obvious that the critical modes are preserved in the ROM. This result is also consistent with the time domain simulation when the *study area* is perturbed by the same fault as in the case of BT. Fig. 12 shows that the ROM behaves very similar to the FOM. The MSE of power and voltage at the PCC as given in Table II.

With regard to stability preservation, although to the knowledge of the authors, there is no guarantee of stability preservation using the ADI method, authors have never found a case in this research where the ROM of wind farm is unstable. Even if a small number of Arnoldi iterations and shift parameters are used, a stable ROM has always been obtained. For instance, when the number of Arnoldi iterations are set to be 10 and 5, while the number of shift parameters are set to be 5, the reduced models with order 6, 18, and 33 are all stable.

The performance comparison above clearly indicates that the ADI based BT is able to attain comparable accuracy to the results of BT. However, the main advantage of ADI iteration is the ability to solve Lyapunov equations efficiently for large scale systems; thus giving rise to a significant reduction in extraction time as given in Table II.

C. Reduced order model using RK

In the RK, it is necessary to provide a set of interpolation points where the moments of FOMs are preserved. It has been suggested in [13] that one can choose the interpolation points from the mirror image of poles of $G(s)$, specially those with the highest residue. For the wind farm model used in this paper, those poles are given in Table. I.

Three scenarios of moment matching shown in Table. III are considered to examine the influence of interpolation points on RK accuracy. The first scenario, RK1, aims to match moments at two critical modes, namely, M3 and M4. In the RK2, more points are added to match the moments of high order system at all critical modes M1-M4. Finally in RK3, a similar scenario to RK2 is considered with addition of some points, which are not the dominant modes, to enhance accuracy of the ROM

TABLE III
INTERPOLATION POINT SCENARIO FOR RK

Scenario	Order	Interpolation points
RK1	8	$8.17 \pm 310.17i$ (P1), $2.72 \pm 64.94i$ (P2)
RK2	20	P1, P2, $58.50 \pm 1979.16i$ (P3), $70.83 \pm 1379.46i$ (P4)
RK3	36	$0, \pm 1i, \pm 10i, \pm 40i$, P1, P2, P3, P4

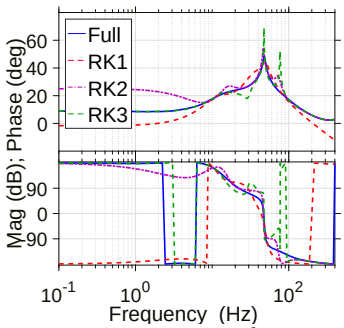

Fig. 13: Bode plot of *external-area* from $\text{Vq}_{\text{pcc}}^{\text{ref}}$ to Id_{pcc}: FOM vs ROM by RK

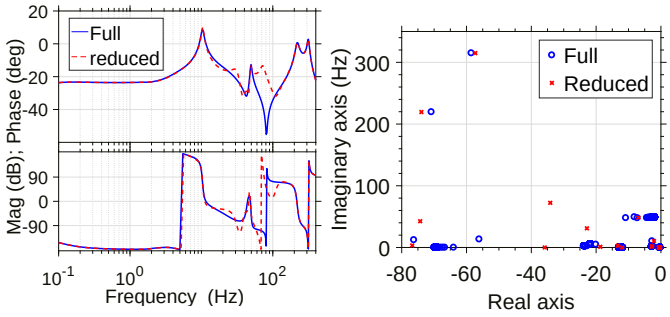

(a) Bode plot from $\text{Vd}_{\text{pcc}}^{\text{ref}}$ to Vq_{pcc} (b) Eigenvalue plot

Fig. 14: Frequency domain comparison of complete system: FOM vs ROM by RK

at low frequency. These scenarios are carefully selected to preserve the stability of the *external-area* as it is well-known that the RK does not preserve stability. Although it is found in this paper that selecting interpolation points from a subset of the negative poles of $G(s)$ often produces a stable ROM, this approach sometimes produces an unstable reduced system. For example, if the interpolation point are $2.72 \pm 64.94i$ (M2) and $70.83 \pm 1379.46i$ (M4), the ROM has two unstable modes.

The Bode plots from $\text{Vq}_{\text{pcc}}^{\text{ref}}$ to Id_{pcc} of the RK1-RK3 are compared to that of the FOM of *external-area* in Fig. 13. Although the both RK1 and RK2 are able to produce accurate Bode plot response at the preselected points, they are erroneous at low frequency range. With the incorporation of interpolation points at low frequency, RK3 produces more accurate results. This shows that the choice of interpolation points significantly affects accuracy of the ROM. For further analysis, RK3 is selected.

The Bode and eigenvalue plots when the RK3 is reconnected to the *study-area* are shown in Fig. 14. Both plots indicate that the ROM is generally able to capture the critical modes of FOM. However, it can be seen that there are small errors in the Bode plot. Further, the time domain simulation is performed by using the same scenario of fault as in the previous sections and the responses of power and voltage at PCC are given in Fig. 15. It is likely that the errors previously shown in the Bode plot might influence accuracy of time-domain simulation. The MSE for both power and voltage at PCC is slightly larger than in the previous cases as indicated in Table. II. Finally, it remains to be seen that the main advantage of RK as shown in Table II is a significant reduction in the extraction time, which accounts only for 0.32 s.

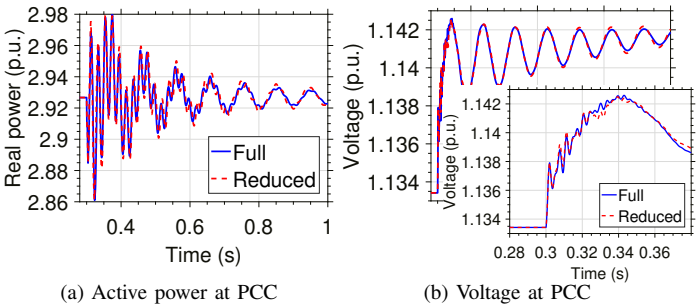

(a) Active power at PCC (b) Voltage at PCC

Fig. 15: Time domain comparison of complete system: FOM vs ROM by RK

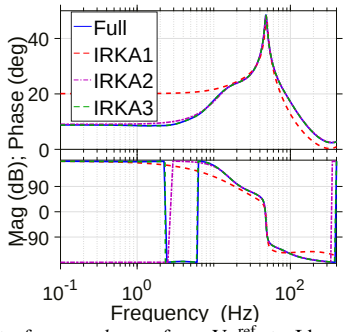

Fig. 16: Bode plot of *external-area* from $\text{Vq}_{\text{pcc}}^{\text{ref}}$ to Id_{pcc}: FOM vs ROM by IRKA

D. Reduced order model using IRKA

The performance of RK methods is determined by selection of the interpolation points, which is often difficult to do. This is exacerbated by the fact that the operating condition of wind farms continuously changes, which in turn affects the dominant modes. With the aim to overcome these difficulties, the iterative rational Krylov algorithm (IRKA) is proposed to reduce the model of wind farm. In this way, a set of initial interpolation points with corresponding tangential directions are updated until an optimal point, which solves (29), is found.

To demonstrate the effectiveness of IRKA, three ROMs, namely, IRKA1, IRKA2, and IRKA3 are considered. These models have the same order as RK1, RK2 and RK3, respectively. The interpolation points with the corresponding right and left tangential directions for these models are selected randomly. Using these random parameters, the IRKA is able to converge within 16, 81, and 23 iterations and requires elapsed time of $2.51s$, $19.41s$, and $7.41s$ for IRKA1, IRKA2, and IRKA3, respectively. There are two stopping criteria adopted in this study, namely, the H_2-norm for interpolation points and reduced system. If any of these criteria falls below the tolerance, then the IRKA iteration stops. The final error for the interpolation points and system are 2.0×10^{-4} and 2.1×10^{-3} for IRKA1, 8.8×10^{-3} and 8.5×10^{-4} for IRKA2, and 2.6 and 8.7×10^{-4} for IRKA3. The Bode plots from $\text{Vq}_{\text{pcc}}^{\text{ref}}$ to Id_{pcc} for these ROMs are compared to that of the FOM of *external-area* in Fig. 16, which in general shows superior performance of the IRKA to the RK. It is also obvious that the IRKA3 produces more accurate results than IRKA1 and IRKA2. For further analysis, only the IRKA3 is considered.

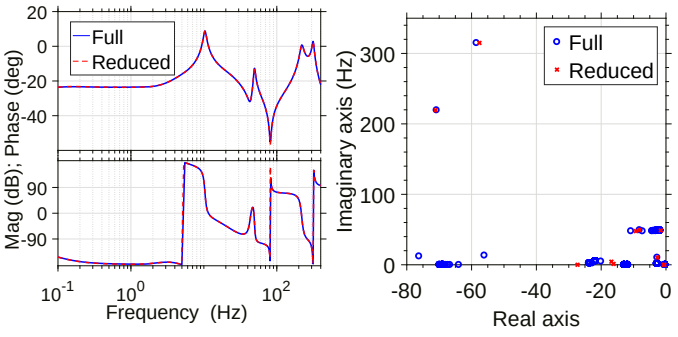

(a) Bode plot from $\text{Vd}_{\text{pcc}}^{\text{ref}}$ to Vq_{pcc} (b) Eigenvalue plot

Fig. 17: Frequency domain comparison of complete system: FOM vs ROM by IRKA

The response of complete ROM with IRKA3 is compared to the responses of FOM. The Bode and eigenvalue plots are given in Fig. 17 and it shows generally better performances of IRKA than RK. This result is also compatible with the time-domain simulation when the system is subjected by the same disturbance as in the previous sections. The power and voltage responses at the PCC are given in Fig. 18 with the corresponding MSE equal to 1.45×10^{-5} and 1.52×10^{-5}, respectively, as shown in Table II. It is to be noted that in term of stability preservation, to the knowledge of authors, the IRKA essentially does not preserve stability of the FOM. This is observed from a large number of experiments that unstable ROMs are sometimes generated from a stable FOM.

E. Reduced order model using Modal Truncation

In this section, application of the SAMDP method to obtain ROM of the wind farm is investigated. Different from the previous methods, it is found that the SAMDP cannot be applied directly to the original linearised model of the *external-area*. It is because there is a problem with eigenvalue conditioning. This can be studied through the condition number of the eigenvector matrix, i.e.

$$\text{cond}(X^v) = \|X^v\|_2 \left\|X^{v-1}\right\|_2 = \|X^v\|_2 \|Y^v\|_2 \tag{34}$$

The original matrix has this number around 1250, which indicates that the eigenvalues are very sensitive to any changes in elements of A, for instance due to rounding error. As the SAMDP calculates explicitly the eigenpair $\{\lambda_i, x_i, y_i\}$, this method cannot converge unless $\text{cond}(X^v)$ is reduced. To do this, a similarity transform is performed,

$$A_{\text{sim}} = T^{-1}AT \tag{35}$$

where A_{sim} has equal row and column norm whenever possible. This is carried out by using a Matlab's command *balance*. Performing this step, $\text{cond}(X^v)$ decreases significantly to 803.80, which in turn enables the SAMDP to converge.

Three scenarios are considered to test the performance of SAMDP, namely SAMDP1 (18 dominant modes), SAMDP2

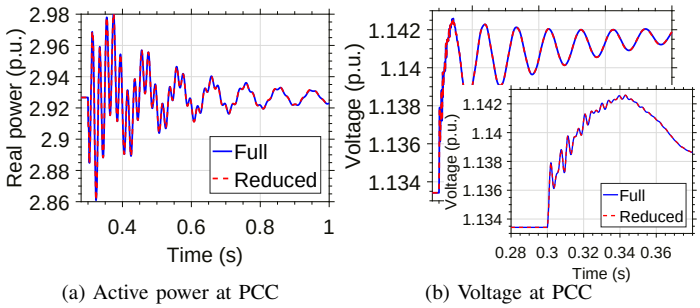

(a) Active power at PCC (b) Voltage at PCC

Fig. 18: Time domain comparison of complete system: FOM vs ROM by IRKA

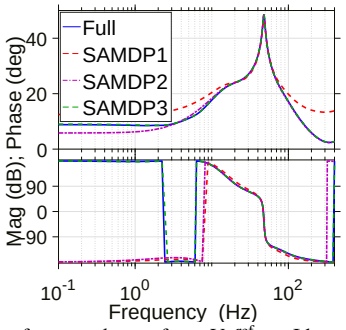

Fig. 19: Bode plot of *external-area* from $\mathrm{Vq}_{\mathrm{pcc}}^{\mathrm{ref}}$ to $\mathrm{Id}_{\mathrm{pcc}}$: FOM vs ROM by SAMDP

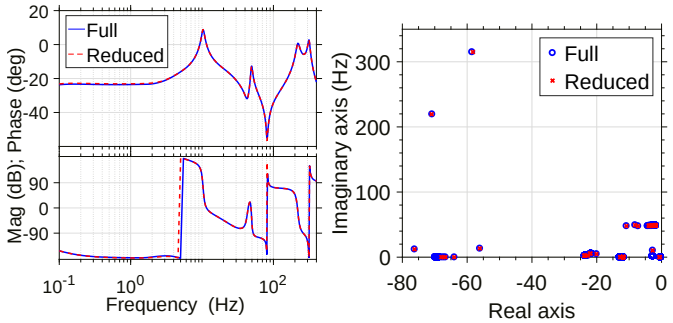

(a) Bode plot from $\mathrm{Vd}_{\mathrm{pcc}}^{\mathrm{ref}}$ to $\mathrm{Vq}_{\mathrm{pcc}}$ (b) Eigenvalue plot

Fig. 20: Frequency domain comparison of complete system: FOM vs ROM by SAMDP

(40 dominant modes), and SAMDP3 (180 dominant modes). The orders of these models are 36, 74, 301 for SAMDP1-SAMDP3, respectively and an initial value of the pole is set to be $1i$ for all cases. The Bode plot from $\mathrm{Vq}_{\mathrm{pcc}}^{\mathrm{ref}}$ to $\mathrm{Id}_{\mathrm{pcc}}$ for these models are compared with that of the FOM of *external-area* in Fig. 19. It is obvious that to improve accuracy of SAMDP, higher number of poles need to be incorporated. Notice that SAMDP requires significantly higher order than the other methods in order to obtain comparable accuracy. It is due to the fact that the SAMDP gives a high priority to the modes whose residues are high. However, it is true that these modes might not be always important for system dynamics; hence selecting these modes does not always improve accuracy of the ROM. Another reason is that the SAMDP extracts all poles which are close each other. The SAMDP3 is selected for further analysis. Fig 20 shows the performance of SAMDP in frequency domain. It is obvious that both the Bode and eigenvalue plot are able to capture the responses of FOM. This translates into time domain performance as illustrated in Fig. 21, where very small errors are observed in the waveform of power and voltage at the PCC. The values of MSE for these plots are given in Table II. Further increase the order should minimise the error further.

There are two important technical details to be discussed. Firstly, the SAMDP is able to efficiently extract 180 modes within only 31.17 s, see Table II. Secondly, due to the fact that the SAMDP extracts the poles of FOM one-at-a-time, stability of ROM is always guaranteed whenever the FOM is stable, which is confirmed by experiments.

V. ROM OF DIFFERENT ORDER OF WIND FARM MODELS

This section presents performance of the MOR methods on different wind farm models. Two new wind farm models are

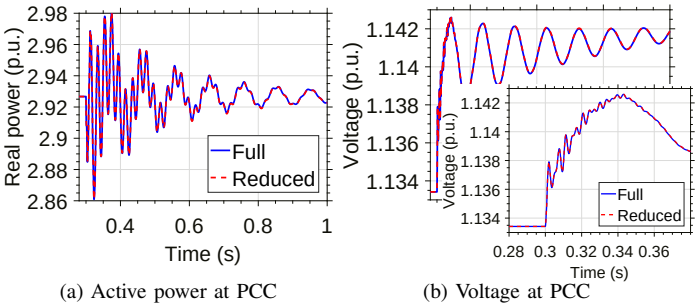

(a) Active power at PCC (b) Voltage at PCC

Fig. 21: Time domain comparison of complete system: FOM vs ROM by SAMDP

TABLE IV
MOR ON DIFFERENT WIND FARM MODELS

Method	Performance	System 1 (2902)	System 2 (3874)	System 3 (6770)
BT	Order	39	39	51
	Extraction	186.42 s	433.00 s	2168.55 s
	MSE P_{PCC}	8.35×10^{-6}	3.77×10^{-4}	2.33×10^{-4}
	MSE V_{PCC}	1.39×10^{-6}	2.96×10^{-4}	1.14×10^{-5}
	MSE Bode	5.29×10^{-4}	8.10×10^{-3}	5.20×10^{-3}
ADI	Order	39	39	51
	Extraction	14.53 s	19.18 s	32.19 s
	MSE P_{PCC}	8.38×10^{-6}	4.80×10^{-5}	2.20×10^{-4}
	MSE V_{PCC}	1.40×10^{-6}	2.05×10^{-6}	1.14×10^{-5}
	MSE Bode	5.30×10^{-4}	6.14×10^{-4}	5.20×10^{-3}
RK	Order	38	42	28
	Extraction	0.23 s	0.32 s	0.31 s
	MSE P_{PCC}	4.02×10^{-4}	4.30×10^{-3}	3.60×10^{-2}
	MSE V_{PCC}	7.78×10^{-6}	9.90×10^{-4}	1.80×10^{-3}
	MSE Bode	2.90×10^{-2}	2.60×10^{-2}	2.50×10^{-1}
IRKA	Order	38	42	28
	Extraction	6.67 s	7.41 s	77.33 s
	MSE P_{PCC}	1.74×10^{-5}	1.45×10^{-5}	7.10×10^{-3}
	MSE V_{PCC}	1.80×10^{-6}	1.52×10^{-5}	4.20×10^{-3}
	MSE Bode	5.90×10^{-4}	2.20×10^{-3}	1.60×10^{-2}
SAMDP	Order	110	307	339
	Extraction	10.13 s	31.17 s	61.90 s
	MSE P_{PCC}	7.18×10^{-4}	2.42×10^{-4}	8.80×10^{-4}
	MSE V_{PCC}	2.54×10^{-5}	1.61×10^{-5}	6.03×10^{-5}
	MSE Bode	3.60×10^{-2}	1.30×10^{-3}	3.10×10^{-3}

obtained from the modification of the wind farm shown in Fig. 1. Firstly, the Wind Farm 2 of Fig. 1 is removed, which yields a new wind farm with an order of 2902. This wind farm has a total of 90 DFIGs and is referred as System 1. Secondly, the Wind Farm 1 of Fig. 1 is duplicated, resulting in a new system with a total of 210 DFIGs and an order of 6770. This system is termed as System 3. The original wind farm model consisting of 90 DFIGs is referred as System 2.

Table IV shows performances of the five methods on the System 1, System 2, and System 3. Note that the results for System 2 are presented again here for the sake of clarity. It is obvious that the BT consistently has the highest computation time for all systems. The increase in computational time of BT is at a rate of around $\mathcal{O}(n^3)$, which stems from solving the Lyapunov equations. This practically limits the use of BT for wind farm MOR. The introduction of ADI method to solve these equations reduces the computational time to approximately $\mathcal{O}(n)$ as evident from Table IV. The accuracy of ADI in all cases is practically similar to that of BT. It is also confirmed that unstable ROMs calculated from ADI are never found in all wind farm models.

Table IV also indicates that the IRKA outperforms the RK in both time and frequency domain for all test systems, but the IRKA requires significantly higher computational time than the RK. This observation is more pronounced as the system

size increases. The computational time of RK in all cases is less than 0.4 s. But, it is to be noted that the RK often produced unstable ROMs and stability preservation becomes more difficult for larger systems. In particular for System 3, the ROM are unstable for many cases and only the reduced model with an order of 28 is stable. For the IRKA, stability for System 3 is essentially also not always preserved. Finally, in order to achieve comparable accuracy to other methods, the SAMDP constantly requires higher order that other methods and always produces stable ROMs.

VI. Conclusions

This paper describes linear MOR techniques for wind farm systems, namely BT, ADI-based BT, RK, IRKA, and SAMDP. The models are practically-sized wind farm systems with 90, 120, and 210 DFIGs. Due to solving Lyapunov equations, the application of BT to the wind farm model is computationally expensive. With the aim of reducing the computational time, the ADI-based BT solves Lyapunov iteratively. This method can attain accuracy of BT at much lower computational cost. In RK, the moments of full order system are retained in the reduced order system at a set of pre-specified interpolation points. These points determine the accuracy of the reduced order model and therefore should be chosen carefully at mirror image of the dominant modes. As the operating condition of wind farms changes, the interpolation points need to be changed accordingly, making this a very difficult task to do. To overcome these problem, the IRKA iteratively calculates a set of initial interpolation points to minimise error between FOM and ROM. Finally, the SAMDP is able to extract the poles of FOM one-at-a-time to construct the ROM, but it strongly depends on the eigenvalue conditioning on systems matrices. Although the comparison between full and reduced order model in term of Bode plot, eigenvalue plot, and and waveform at the PCC show that all methods can provide an acceptable reduced order model, it seems that IRKA is the most suitable method for large-scale wind farm applications. This is due to the fact that IRKA is able to provide a very accurate model within reasonable extraction time and order. Furthermore, IRKA is also less sensitive to initial parameter set up.

Appendix A
Solving linear equations using ADI iteration

let's define a linear system of equations [19],

$$Ax = b \tag{36}$$

with A being a symmetric positive definite matrix. Matrix A can be factorized as a sum of two positive definite matrices, L and R. As a result, (36) can be rewritten as $Lx+Rx = b$. This equation can be solved using ADI iteration by performing the following routines,

$$\begin{aligned}(L + \alpha_i I_n)x_{i-\frac{1}{2}} &= (\alpha_i I_n - R)x_{i-1} + b \\ (R + \alpha_i I_n)x_i &= (\alpha_i I_n - R)x_{i-\frac{1}{2}} + b\end{aligned} \tag{37}$$

where α_i are ADI shift parameters. A careful selection of these parameter is critical for ADI iteration to converge to the solution x.

Acknowledgment

The first author fully acknowledges the Indonesia Endowment Fund for Education (LPDP) scholarship, Ministry of Finance, The Republic of Indonesia for funding his PhD research at Imperial College London. The authors would also like to acknowledge Dr. Nelson Martins of CEPEL for providing technical discussion on the SAMDP method.

References

[1] "Global wind report; annual market update," *Global Wind Energy Council*, 2016.

[2] K. Zhou and J. C. Doyle, *Essentials of robust control*. Prentice hall Upper Saddle River, NJ, 1998, vol. 180.

[3] J. Slootweg and W. Kling, "Aggregated modelling of wind parks in power system dynamics simulations," in *Power Tech Conf Proc, 2003 IEEE Bologna*, vol. 3. IEEE, 2003, pp. 6–pp.

[4] M. Ali, I.-S. Ilie, J. V. Milanovic, and G. Chicco, "Wind farm model aggregation using probabilistic clustering," *Power Sys, IEEE Trans on*, vol. 28, no. 1, pp. 309–316, 2013.

[5] J. Zou, C. Peng, H. Xu, and Y. Yan, "A fuzzy clustering algorithm-based dynamic equivalent modeling method for wind farm with DFIG," *IEEE Trans on Energy Conv*, vol. 30, no. 4, pp. 1329–1337, Dec 2015.

[6] L. P. Kunjumuhammed, B. C. Pal, C. Oates, and K. J. Dyke, "Electrical oscillations in wind farm systems: Analysis and insight based on detailed modeling," *Sustainable Energy, IEEE Trans on*, no. 1, pp. 51–62, 2016.

[7] B. C. Moore, "Principal component analysis in linear systems: Controllability, observability, and model reduction," *Automatic Control, IEEE Transactions on*, vol. 26, no. 1, pp. 17–32, 1981.

[8] A. C. Antoulas, *Approximation of large-scale dynamical systems*. Siam, 2005, vol. 6.

[9] F. D. Freitas, J. Rommes, and N. Martins, "Gramian-based reduction method applied to large sparse power system descriptor models," *IEEE Transactions on Power Systems*, vol. 23, no. 3, pp. 1258–1270, 2008.

[10] M. Heinkenschloss, D. C. Sorensen, and K. Sun, "Balanced truncation model reduction for a class of descriptor systems with application to the oseen equations," *SIAM Journal on Scientific Computing*, vol. 30, no. 2, pp. 1038–1063, 2008.

[11] E. J. Grimme, "Krylov projection methods for model reduction," Ph.D. dissertation, University of Illinois at Urbana-Champaign, 1997.

[12] S. Gugercin, C. Beattie, and A. Antoulas, "Rational Krylov methods for optimal H_2 model reduction," *submitted for publication*, 2006.

[13] S. Gugercin and A. Antoulas, "An H_2 error expression for the Lanczos procedure," in *Decision and Control, 2003. Proceedings. 42nd IEEE Conference on*, vol. 2. IEEE, 2003, pp. 1869–1872.

[14] J. Rommes and N. Martins, "Efficient computation of multivariable transfer function dominant poles using subspace acceleration," *IEEE transactions on power systems*, vol. 21, no. 4, pp. 1471–1483, 2006.

[15] L. P. Kunjumuhammed, B. C. Pal, R. Gupta, and K. J. Dyke, "Stability analysis of a PMSG-based large offshore wind farm connected to a VSC-HVDC," *IEEE Transactions on Energy Conversion*, vol. 32, no. 3, pp. 1166–1176, 2017.

[16] J. H. Chow, *Power sys. coherency and model reduction*. Springer, 2013.

[17] C.-T. Chen, *Linear sys. theory and design*. Oxford Univ Press,Inc., 1995.

[18] K. Glover, "All optimal Hankel-norm approximations of linear multivariable systems and their L_∞ error bounds," *Intl journal of control*, vol. 39, no. 6, pp. 1115–1193, 1984.

[19] P. Kürschner, "Efficient low-rank solution of large-scale matrix equations," Ph.D. dissertation, Shaker Verlag Aachen, 2016.

[20] T. Penzl, "A cyclic low-rank Smith method for large sparse Lyapunov equations," *SIAM Journal on Scientific Computing*, vol. 21, no. 4, pp. 1401–1418, 1999.

[21] E. L. Wachspress, *The ADI model problem*. Springer, 2013.

[22] K. Gallivan, A. Vandendorpe, and P. Van Dooren, "Model reduction of MIMO systems via tangential interpolation," *SIAM Journal on Matrix Analysis and Applications*, vol. 26, no. 2, pp. 328–349, 2004.

[23] "[online:]," *http://w3.onera.fr/more/?q=teaching*, accessed 14/08/2017.

[24] P. Van Dooren, K. A. Gallivan, and P.-A. Absil, "H_2-optimal model reduction of MIMO systems," *Applied Mathematics Letters*, vol. 21, no. 12, pp. 1267–1273, 2008.

[25] A. Castagnotto, M. C. Varona, L. Jeschek, and B. Lohmann, "sss & sssMOR: Analysis and reduction of large-scale dynamic systems in MATLAB," *at-Automatisierungstechnik*, vol. 65, no. 2, pp. 134–150, 2017.